Accuracy of the Skin Depth Correction for Metallic Nanoparticle Polarizability

Weilin Liu and Euan McLeod*

College of Optical Sciences, University of Arizona, Tucson, Arizona 85719, USA

E-mail: euanmc@optics.arizona.edu

Abstract

Dipole approximations are commonly used in calculations of light scattering and optical forces acting on nanoparticles. The scattered field strength is proportional to particle volume. For the past three decades, many researchers have used an effective volume based on skin depth when dealing with metallic nanoparticles, instead of the full volume. By comparing several dipole models to Mie scattering and finite difference time domain simulations, we show that it is more accurate to use the full volume because the complex relative permittivity of the metal already accounts for its skin depth.

Introduction

Light scattering calculations play a key role in many areas including aerosol analysis, photovoltaics, spectroscopy, biosensing, atomic trapping, and optical tweezers, among others ^{1–11}. For spherical particles, the gold standard approach is to use Mie scattering ¹², however these calculations can be cumbersome and tedious. For particles much smaller than the wavelength of light, a simpler approach is to use Rayleigh scattering calculations, which assume that a particle can be approximated as a single dipole, with induced relative dipole moment,

$$\mathbf{p} = \varepsilon_b \alpha \mathbf{E}_{inc}(\mathbf{r}_0), \tag{1}$$

where ε_b is the relative permittivity of the background media, α is the polarizability of the particle, and $\mathbf{E}_{inc}(\mathbf{r}_0)$ is the incident electric field evaluated at the center of the particle. The polarizability of the particle can be approximated by the Clausius-Mossotti (CM) relation ¹³:

$$\alpha_{\rm CM} = 3\varepsilon_0 V \frac{\varepsilon - \varepsilon_b}{\varepsilon + 2\varepsilon_b} \tag{2}$$

where ε_0 is the permittivity of free-space, $\varepsilon = \varepsilon' + i\varepsilon''$ is the complex permittivity of the particle, $V = (4/3)\pi a^3$ is the spherical particle volume, and a is particle radius. The CM

relation (eq 2) is widely accepted for both dielectric and metallic particles as the particle size tends to zero, while for particles much larger than the wavelength, the dipole approximation fails in general. In 1994, Svoboda and Block¹⁴ proposed an effective volume correction $(V \to V_{\text{eff}})$ to increase the range of validity of eq 2 specifically for particles whose radii are not much smaller than the material skin depth, $\delta = \lambda/(2\pi n'')$, where $n'' = \text{Im}\{\varepsilon^{1/2}\}$ is the imaginary part of the refractive index of the material, assuming unit relative magnetic permeability. V_{eff} was given by,

$$V_{\text{eff}} = 4\pi \int_0^a r^2 e^{\frac{r-a}{\delta}} dr. \tag{3}$$

Metallic skin depths are typically a few tens of nanometers at optical wavelengths, effectively limiting the interaction volume between the light and particle to a small shell near the surface of the particle. Based on this skin depth effect, it was anticipated that particles of size $a \ll \delta$ would exhibit a trapping force proportional to the total particle volume ($\propto a^3$), while particles with $a \gg \delta$ would exhibit a trapping force proportional to the shell volume ($\propto a^2$).

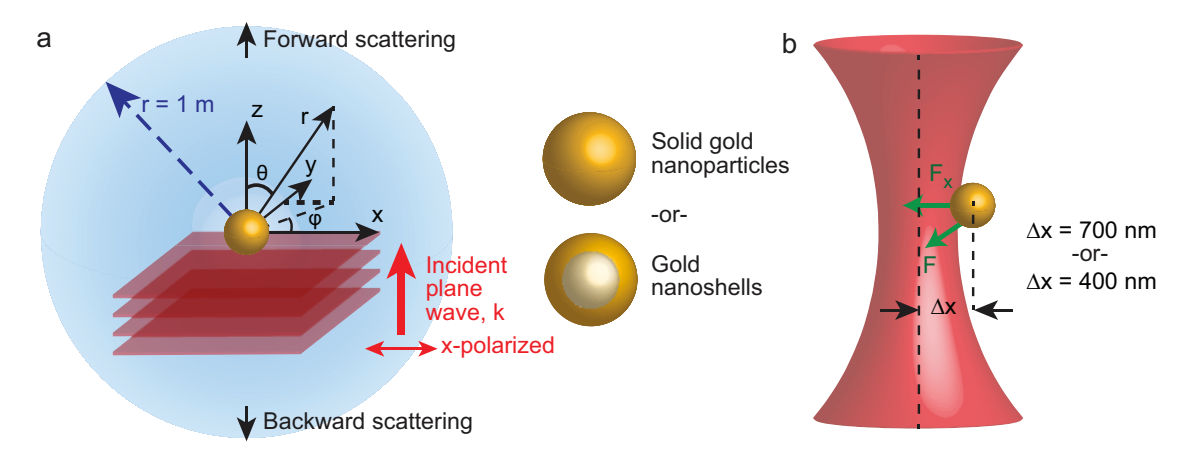


Figure 1: Simulation geometry. (a) Far field scattering calculations are performed for solid and hollow gold nanospheres illuminated by plane waves. (b) Optical force calculations are performed on gold nanospheres displaced laterally by Δx from the optical axis of a Gaussian beam with $\lambda/2$ beam waist.

Several experimental studies have investigated the dependence of trap force on particle size, but have typically found a rapid transition in trapping force scaling from a^3 to sig-

nificantly slower than a^2 without any clearly identifiable region of a^2 scaling for spherical particles^{15–18} and non-spherical particles¹⁹. A qualitative explanation was that that the reduced trapping forces were due to enhanced radiation pressure forces displacing the particles away from the beam focus^{15,20}. One experimental study stated that a region of a^2 dependence can be found by minimizing the spherical aberration in the system, but this was based on a fit to only four data points²¹. Despite the dearth of experimental evidence supporting the volume correction approach based on skin depth, it has continued to be used by many different groups, including our own^{16,21–31}.

In this Article we show that while the concept of the skin depth is physically accurate, the commonly-used volume correction factor in eq 3 is inaccurate, and in fact, the skin depth effect is best accounted for by simply using the complex-valued ε . We show that far-field scattering and optical force calculations (Figure 1) are more accurate using the full particle volume than a corrected effective volume. And for particles larger than $\lambda/10$, the optical force is neither proportional to the shell volume nor the total particle volume.

Computational Details

Polarizability Models

We compare the accuracy of four different expressions for polarizability: the basic CM relation (eq 2), the CM relation with radiation reaction (RR) correction, the effective volume approach based on skin depth (SD), and the effective volume approach combined with radiation reaction (SDRR). The radiation reaction corrects for the back-action of the scattered field on the dipole moment, and can be expressed as ³²,

$$\alpha_{\rm RR} = \alpha_{\rm CM} \left[1 - \frac{ik^3}{6\pi\varepsilon_0} \alpha_{\rm CM} \right]^{-1},\tag{4}$$

where $k = 2\pi n_b/\lambda$ is the wavenumber and n_b is the refractive index of the background medium. Note that in the small particle / large wavelength limit, the radiation reaction correction factor only becomes significant at intermediate particle sizes ($\lambda/50 < a < \lambda/2$). When using an effective volume based on the skin depth, the polarizability can be expressed as,

$$\alpha_{\rm SD} = \frac{V_{\rm eff}}{V} \alpha_{\rm CM}.\tag{5}$$

Finally, by combining the effective volume and radiation reaction corrections, the polarizability is

$$\alpha_{\rm SDRR} = \alpha_{\rm SD} \left[1 - \frac{ik^3}{6\pi\varepsilon_0} \alpha_{\rm SD} \right]^{-1}. \tag{6}$$

Forward and Backward Scattering

We compare these polarizabilities using a far-field scattering analysis from plane wave excitation, as shown in Figure 1a. In the far field, the light scattered or radiated by an oscillating dipole is purely transverse and its components are given by ³³,

$$\mathbf{E}_{s} = \begin{bmatrix} E_{\theta} \\ E_{\phi} \end{bmatrix} = \frac{k^{2}}{4\pi\varepsilon_{0}\varepsilon_{b}} \frac{e^{ikr}}{r} \begin{bmatrix} (p_{x}\cos\phi + p_{y}\sin\phi)\cos\theta - p_{z}\sin\theta \\ -p_{x}\sin\phi + p_{y}\cos\phi \end{bmatrix}, \tag{7}$$

where p_x , p_y , and p_z are the Cartesian components of \mathbf{p} ; θ is the polar angle from the z-axis; and ϕ is the azimuthal angle.

We use Mie theory as the gold standard, rigorous solution for the diffraction of a monochromatic plane wave perturbed by an isotropic, homogeneous sphere. It is valid for particles of any diameter and composition. We compute scattered fields using the Mie therory formalism presented by Born & Wolf³⁴. The Mie series solution is truncated after 14 terms, which is enough for convergence for spheres throughout the size range investigated here.

In addition to Mie scattering calculations of the far field intensity, we also rely on finitedifference time-domain (FDTD) simulations as a trusted computational approach. These simulations are implemented in Lumerical's FDTD Solutions software with a stability factor of 0.99, an auto shut-off minimum of 10^{-5} , vacuum background, and perfectly matched layers (PML) in all boundary conditions. The far field scattering intensity can be obtained using the "Total Field Scattered Field" source option. With this option, the E-field scattered from a particle onto a closed box of 6 rectangular monitors is computed. Then the far-field scattering distribution can be reconstructed using the surface equivalence theorem³⁵. After summing up the product of the electric near-field and the surface normals of the closed box, the results are projected to a closed spherical surface with 1 m radius in the far-field. We implement this reconstruction using both Lumerical's built-in script and Matlab.

Optical Forces

The optical force exerted on a solid gold nanosphere illuminated by a monochromatic xpolarized Gaussian beam is investigated using the configuration in Figure 1b. The gold
nanosphere is displaced 0.7 μ m laterally from the center of beam waist at 1064 nm excitation
and 0.4 μ m laterally from the center of beam waist at 550 nm excitation. Within the dipole
approximation, the time-averaged optical force can be calculated from the polarizability as 33 ,

$$\langle \mathbf{F} \rangle = \frac{1}{2} \sum_{j} \operatorname{Re} \{ \alpha^* E_{\text{inc},j}^* \nabla E_{\text{inc},j} \}$$
 (8)

where $E_{\text{inc},j}$ is the j^{th} Cartesian component of the incident electric field and * represents complex conjugate. Here we determine the incident electric field through FDTD simulations of the focused Gaussian beam without any particle in the domain with 0.5 nm \times 0.5 nm grid size.

We compare the forces predicted by the dipole model to trusted Maxwell's stress tensor (MST) calcultions by computing, ³³

$$\langle \mathbf{F} \rangle = \int_{\partial V} \langle \overrightarrow{\mathbf{T}}(\mathbf{r}, t) \rangle \cdot \hat{\mathbf{n}}(\mathbf{r}) dA,$$
 (9)

where $\hat{\mathbf{n}}(\mathbf{r})$ is the surface normal, and the MST is given by

$$\overleftarrow{\mathbf{T}} = \varepsilon_0 \varepsilon_b \mathbf{E} \otimes \mathbf{E} + \mu_0 \mu_b \mathbf{H} \otimes \mathbf{H} - \frac{1}{2} (\varepsilon_0 \varepsilon_b E^2 + \mu_0 \mu_b H^2) \overleftarrow{\mathbf{T}}, \tag{10}$$

where \otimes represents the tensor product, μ_0 is the free-space permeability, μ_b is the background medium relative permeability, $\overrightarrow{\mathbf{I}}$ is the identity matrix, and \mathbf{E} and \mathbf{H} are the total (incident + scattered) fields, which can be recorded by a cubic monitor enclosing the particles in FDTD simulations. The same stability factor, auto shut-off minimum, background, and boundary conditions are used in these simulations as in the far-field scattering simulations described above.

Results & Discussion

Far Field Scattering

In Figure 2, we compare the intensities of the forward and backward scattered fields computed by Mie theory to the results of dipole models calculated using eqs 1 and 7, with the four different polarizabilities given by eqs 2, 4, 5, and 6 at two wavelengths: 1064 nm and 550 nm. In the dipole models, there is no difference between forward and backward scattering. For 1064 nm excitation, the CM dipole model closely tracks the Mie theory for particles of radius a < 150 nm. However it is important to note that the log scale can somewhat distort the apparent accuracy; the scattered intensity predicted by the CM relation and radiation reaction are only within 5% of both the forward and backward scattered Mie intensity for a < 20 nm, and within 10% for a < 100 nm. Including the radiation reaction correction extends the regime of $\pm 10\%$ accuracy slightly to a < 110 nm. The two models involving a skin depth correction factor are both less accurate than the other dipole models for all particles with radius a < 200 nm, while for a > 200 nm, none of the dipole models accurately describe the scattering.

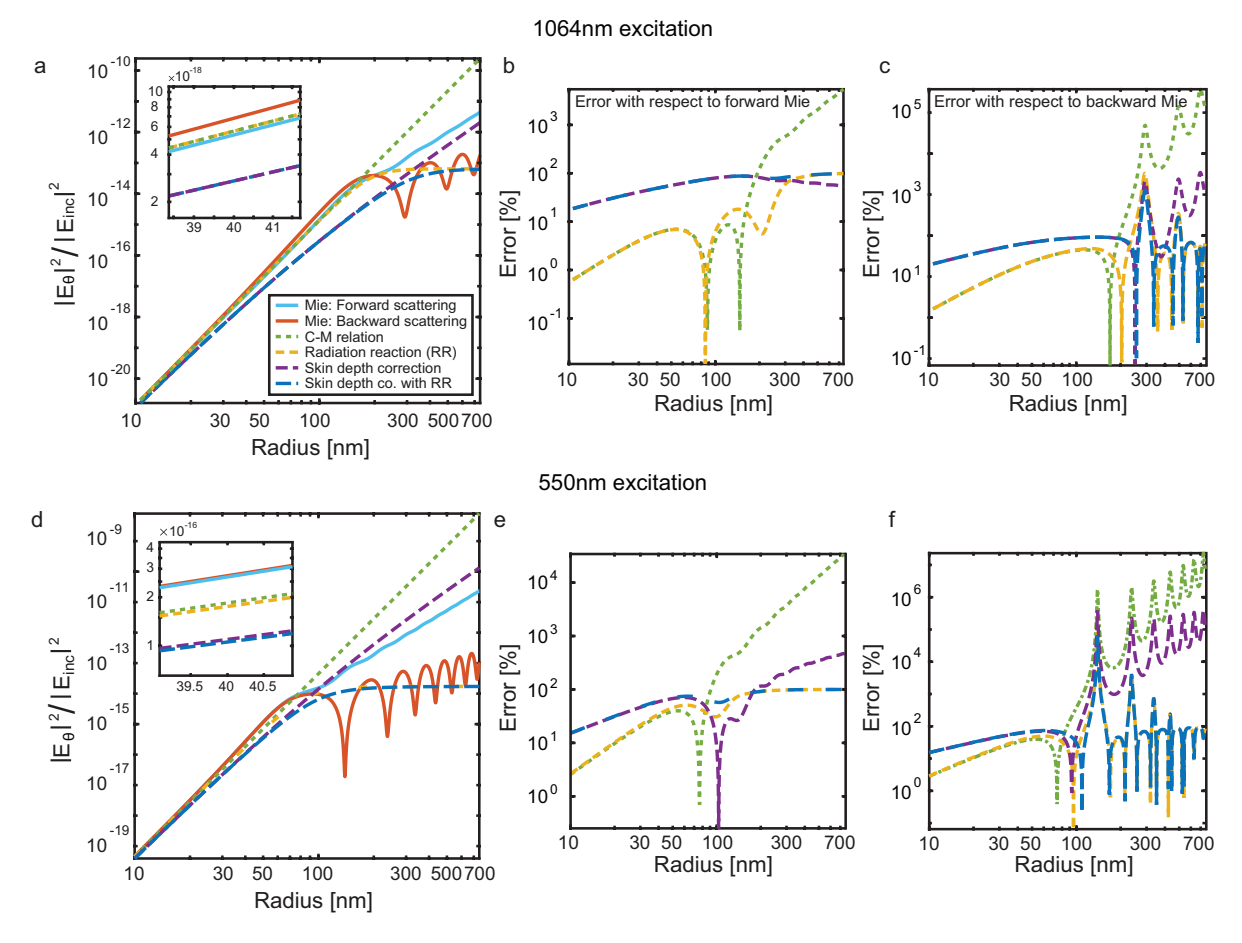


Figure 2: Comparison of far-field scattering models. The Mie theory is treated as the gold standard, with different scattering intensities in the forward and backward directions. (a) Far-field scattering intensity for $\lambda = 1064$ nm. (b) The errors of the four dipole models with respect to forward Mie intensity. (c) The errors of the four dipole models with respect to backward Mie intensity. (d–e) Same as (a–c), but for $\lambda = 550$ nm.

For 550 nm excitation, the scattered intensity predicted by the CM relation and radiation reaction are only within 10% of both the forward and backward scattered Mie intensity for a < 20 nm. The scattered intensities computed by the two dipole models that use an effective volume correction have more than 10% error for all radii simulated except for a crossover point around $a \approx 100$ nm. We also notice that the error between the dipole models and our gold standard is slightly greater at 550 nm excitation than it is at 1064 nm excitation, even when normalizing the particle radius by the wavelength. For example, the radiation reaction model of 10 nm ($\lambda/55$) radius particles exhibits an error of 2.7% at 550 nm, while

the same model of 19 nm ($\lambda/55$) radius particles exhibits an error of 1.9% at 1064 nm. So, much of the error can be captured by simply using a scale factor, although there is also some additional complexity. In summary, it appears that the effective volume correction based on the skin depth is not a particularly good model in any regime, for either wavelength.

The skin depth is, however, a real phenomenon for these particle sizes. The refractive index of gold given by Johnson and Christy³⁶ is n = n' + in'' = 0.26 + 6.97i at 1064 nm. The skin depth can be evaluated as $\delta = 24.3$ nm. Therefore, we can expect that the electric displacement field (D-field) completely fills a 30 nm diameter gold nanosphere, but only exists at the vicinity of the surface for a 300 nm gold sphere, which is consistent with our FDTD simulation in Figure 3. The apparent skin depth in these simulations agrees well with the expected skin depth of 24.3 nm.

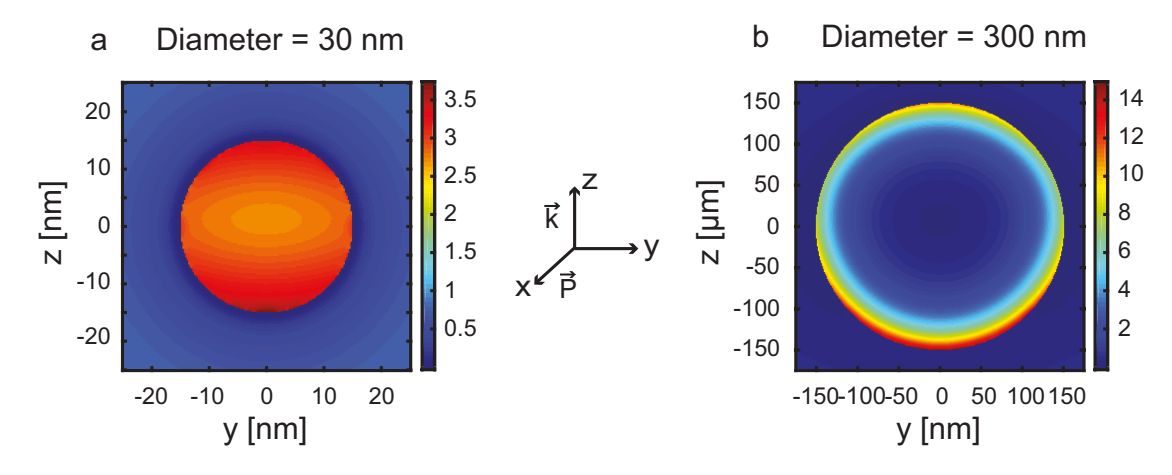


Figure 3: Skin effect at 1064 nm excitation. a shows the D-field distribution in a gold nanosphere with 30 nm diameter. b shows the D-field distribution in a gold nanosphere with 300 nm diameter. In both cases, the unit of D-field is pC/m² and the fields are computed in response to an incident plane wave of amplitude 1 V/m. The FDTD grid sizes used in calculating this figure are a/150 and a/300, respectively.

The skin depth phenomenon can also be verified by investigating whether the light scattered by hollow gold nanoshells is equal to the light scattered by solid gold spheres (Figure 1a) at 1064 nm. We select a shell inner radius a_{eff} such that the total volume of the shell is equal to the effective volume (eq 3) of a solid particle of the same outer radius:

$$\frac{4}{3}\pi a^3 - \frac{4}{3}\pi a_{\text{eff}}^3 = V_{\text{eff}}.$$
 (11)

Meanwhile, the far field intensity in the dipole model can be calculated using eq 7 with the different polarizability models.

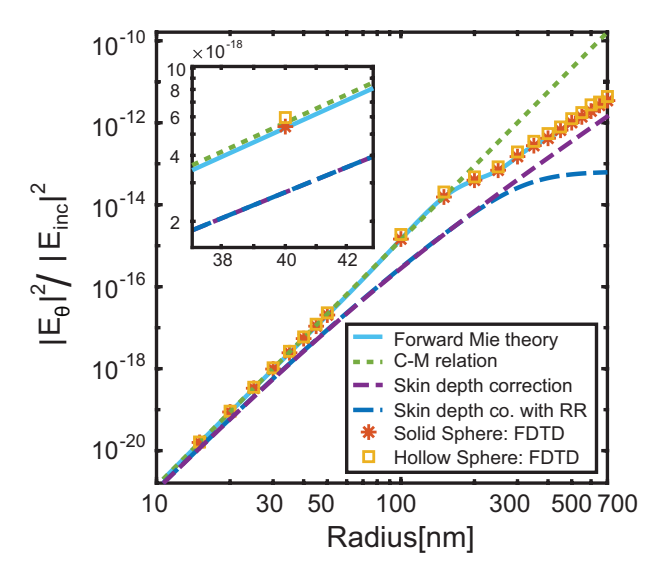


Figure 4: Forward scattering from solid and hollow spheres. The FDTD simulation results for both solid and hollow spheres closely track the solid sphere Mie theory. In the FDTD simulations, the computational grid sizes were in the range of [a/190, a/30] to ensure accuracy. The CM approximation holds for small particles, while the SDRR approximation performs poorly.

Figure 4 shows that the far-field diffraction from the solid sphere computed using FDTD agrees closely with the Mie theory. The hollow sphere results are reasonably close to the solid sphere results, which indicate only a small contribution of the central core of the particle past the skin depth to the scattered field. This supports the existence of the skin depth phenomenon. However, upon closer inspection of the inset of Figure 4, we note that there is some difference between the results of the solid and hollow spheres, indicated by the fact that the two are not precisely optically equivalent. We note that the two dipole models containing an effective volume correction (blue and purple dashed lines) do not accurately

describe either the solid gold particle or the gold shell.

Optical Forces

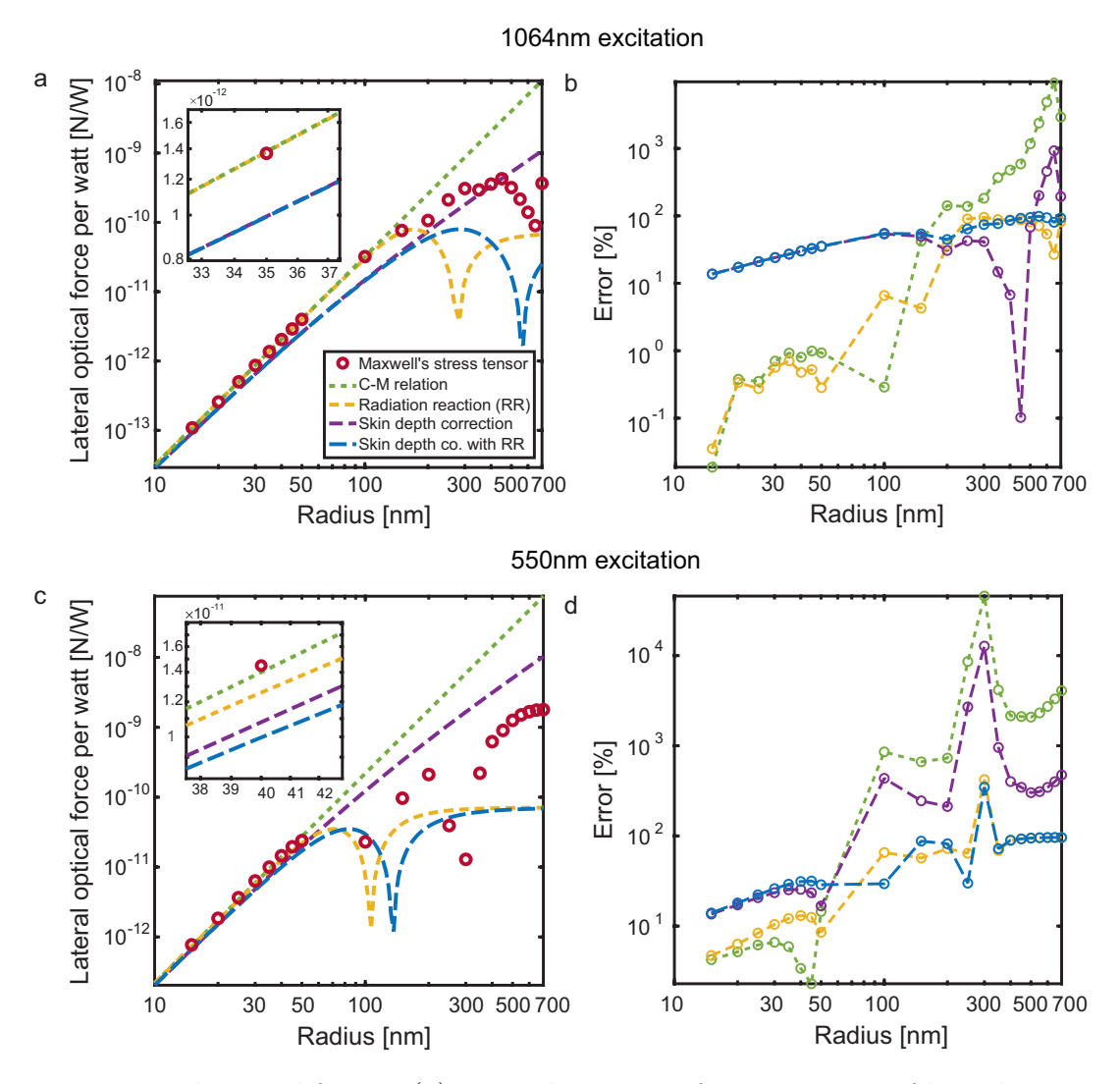


Figure 5: Lateral optical forces. (a) Lateral restoring force per watt of laser beam power at 1064 nm. (b) Relative error of the dipole models with respect to the MST calculation. (c and d) Same as (a) and (b), but with $\lambda = 550$ nm. Out of the various dipole models, the CM relation and CM relation with radiation reaction agree best with the MST calculations for particles with radii $a < \lambda/10$.

Because the effective volume correction (eq 3) appears to have been most frequently applied within the optical trapping community, we also investigate its accuracy in predicting the optical force on gold nanoparticles, as illustrated in Figure 1b. The comparison of

the optical forces predicted by the dipole models to those predicted by the trusted MST calculations are shown in Figure 5. For 1064 nm excitation, the CM relation and radiation reaction dipole models agree well with the MST calculation for a < 100 nm, while the effective volume skin depth models diverge significantly for a > 15 nm. For a > 200 nm, the CM relation and radiation reaction dipole models no longer track the MST calculation. Surprisingly, the skin depth model without radiation reaction is accurate for 200 nm < a <400 nm, but we view this as a purely empirical coincidence because it begins to deviate from the MST again for a > 400 nm. It is important to note that a conventional focused Gaussian beam optical tweezer does not provide a stable 3D trap for such large gold particles with size a > 200 nm, and so an approximate dipole model at this size range may not have significant practical application. Under 550 nm excitation, for a < 50 nm, the error in optical force predicted by the CM relation and radiation reaction dipole models are within 10%, and are more accurate than the two dipole models that invoke an effective volume correction. For a > 50 nm, no model tracks the MST calculation. For the CM relation and radiation reaction dipole models, their errors are slightly larger at 550 nm than at 1064, even when normalizing the particle size by the wavelength. This small difference in errors could be due to increased numerical dispersion error in the FDTD simulations at shorter wavelengths.

In Figure 6, we investigate the magnitude of the total force on the particle at 1064 nm excitation, as opposed to just the lateral force shown in Figure 5. Unlike the lateral force, the total force shows two clear power-law scaling regions as a function of particle radius, with a turning point at $a \approx \lambda/10$. For small particles, the fitted exponent is 3.03 with a 95% confidence interval of [3.00, 3.06] based on the first nine MST calculations. Hence, under the dipole limit, the force is approximately proportional to a^3 , as expected from the CM relation. The fitted slope of Region 2 is computed from eleven different MST calculations, and is found to be 1.37 with 95% confidence interval [1.31, 1.42]. This value differs significantly from the a^2 dependence predicted by a shell-based model with a constant thickness equal to the skin depth, which further confirms that an effective volume based on a shell volume

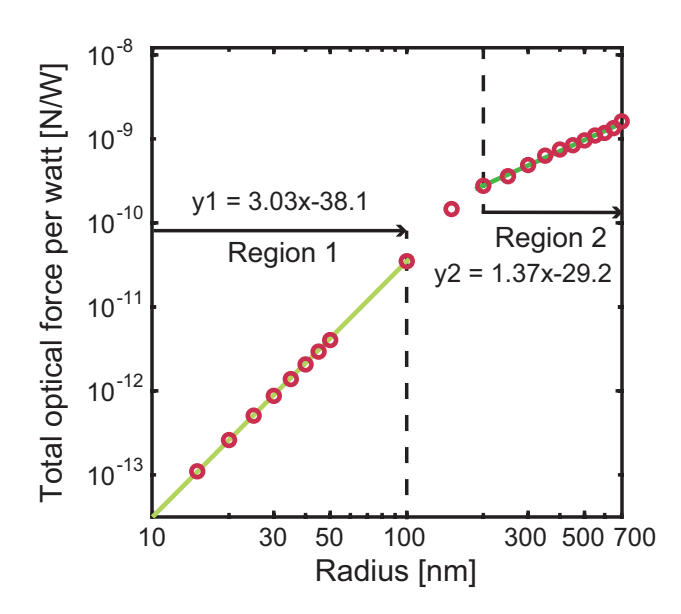


Figure 6: MST calculations of the magnitude of the total optical force per watt of laser beam power. There are two distinct regions of power-law scaling corresponding to $F \propto a^{3.03}$ and $F \propto a^{1.37}$.

does not provide an accurate approximation. These results agree with previous experiments that found that the power law dependence for particles larger than skin depth is less than quadratic ^{15–17}.

We also also investigated the total force on a particle under 550 nm excitation and found similar fitted slopes when the particle is placed near the location of maximal lateral force $(\Delta x = 400 \text{ nm})$. The fitted slope of Region 1 is 3.31 with a 95% confidence interval of [3.21, 3.40] based on the first eight MST calculations. We believe that the deviation from a slope of exactly 3 is due to the increased errors in the dipole approximation at smaller wavelength relative to particle size. The fitted slope of Region 2 is computed from eleven different MST calculations, and is found to be 1.18 with 95% confidence interval [1.08, 1.28].

When using a dipole model to compute the forces on small nanoparticles (10 nm \leq 100 nm), we find that the radiation reaction correction is quite significant in calculating the radiation pressure (scattering) forces, but is less significant for calculating gradient forces. Without the radiation reaction correction, the error in radiation pressure forces are greater than 20%, even for 15 nm radius particles. This is because the radiation pressure force

 $\propto \alpha''$, and for gold at near-IR wavelengths, the value of α'' is primarily derived from radiation reaction and not the bulk material properties. Interestingly, the radiation reaction correction can lead to forces with apparent scaling exponents greater than 3 for intermediate size particles that agrees with MST and FDTD simulation results for this force component. However, in Figure 6, we do not see this effect because the total force on the particle is dominated by the gradient force.

Conclusions

The skin depth effect is observable in simulations; however, the use of an effective volume approach in calculating polarizability is not accurate. Overall, when a dipole approximation can be used, the CM relation with radiation reaction provides the most accurate model of the scattered far-field and optical force. We believe that the effective volume approach is inaccurate because a complex-valued ε already fully accounts for the attenuation of the field within the skin of the particle.

Acknowledgement

This material is based upon work supported by the National Science Foundation under Grant No. ECCS-1807590. W.L. was also supported by FOTO Mayo Family Graduate Scholarship.

References

(1) Derkacs, D.; Lim, S. H.; Matheu, P.; Mar, W.; Yu, E. T. Improved performance of amorphous silicon solar cells via scattering from surface plasmon polaritons in nearby metallic nanoparticles. Applied Physics Letters 2006, 89, 093103.

- (2) Butet, J.; Russier-Antoine, I.; Jonin, C.; Lascoux, N.; Benichou, E.; Brevet, P.-F. Sensing with multipolar second harmonic generation from spherical metallic nanoparticles.

 Nano Letters 2012, 12, 1697–1701.
- (3) Sonnichsen, C.; Geier, S.; Hecker, N. E.; von Plessen, G.; Feldmann, J.; Ditlbacher, H.; Lamprecht, B.; Krenn, J. R.; Aussenegg, F. R.; Chan, V. Z.-H. et al. Spectroscopy of single metallic nanoparticles using total internal reflection microscopy. *Applied Physics Letters* 2000, 77, 2949–2951.
- (4) Cooke, D. D.; Kerker, M. Response calculations for light-scattering aerosol particle counters. *Applied Optics* **1975**, *14*, 734–739.
- (5) Ashkin, A.; Dziedzic, J. M.; Bjorkholm, J. E.; Chu, S. Observation of a single-beam gradient force optical trap for dielectric particles. *Optics Letters* **1986**, *11*, 288–290.
- (6) Padgett, M.; Bowman, R. Tweezers with a twist. *Nature Photonics* **2011**, *5*, 343–348.
- (7) McLeod, E.; Arnold, C. B. Array-based optical nanolithography using optically trapped microlenses. *Optics Express* **2009**, *17*, 3640–3650.
- (8) Xiong, Z.; Melzer, J. E.; Garan, J.; McLeod, E. Optimized sensing of sparse and small targets using lens-free holographic microscopy. *Optics Express* **2018**, *26*, 25676–25692.
- (9) Mcleod, E.; Arnold, C. B. Subwavelength direct-write nanopatterning using optically trapped microspheres. *Nature Nanotechnology* **2008**, *3*, 413–417.
- (10) McLeod, E.; Nguyen, C.; Huang, P.; Luo, W.; Veli, M.; Ozcan, A. Tunable vapor-condensed nanolenses. *ACS Nano* **2014**, *8*, 7340–7349.
- (11) Guffey, M. J.; Scherer, N. F. All-optical patterning of Au nanoparticles on surfaces using optical traps. *Nano Letters* **2010**, *10*, 4302–4308.
- (12) Mie, G. Beitrge zur optik trber medien, speziell kolloidaler metallsungen. Annalen der Physik 1908, 330, 377–445.

- (13) Kittel, C.; Holcomb, D. F. Introduction to solid state physics. *American Journal of Physics* **1967**, *35*, 547–548.
- (14) Svoboda, K.; Block, S. M. Optical trapping of metallic Rayleigh particles. *Optics Letters* **1994**, *19*, 930–932.
- (15) Hansen, P. M.; Bhatia, V. K.; Harrit, N.; Oddershede, L. Expanding the optical trapping range of gold nanoparticles. *Nano Letters* **2005**, *5*, 1937–1942.
- (16) Bosanac, L.; Aabo, T.; Bendix, P. M.; Oddershede, L. B. Efficient optical trapping and visualization of silver nanoparticles. *Nano Letters* **2008**, *8*, 1486–1491.
- (17) Jauffred, L.; Taheri, S. M.-R.; Schmitt, R.; Linke, H.; Oddershede, L. B. Optical trapping of gold nanoparticles in air. *Nano Letters* **2015**, *15*, 4713–4719.
- (18) Saija, R.; Denti, P.; Borghese, F.; Marag, O. M.; Iat, M. A. Optical trapping calculations for metal nanoparticles. Comparison with experimental data for Au and Ag spheres.

 Optics Express 2009, 17, 10231–10241.
- (19) Brzobohat, O.; iler, M.; Trojek, J.; Chvtal, L.; Karsek, V.; Zemnek, P. Non-spherical gold nanoparticles trapped in optical tweezers: shape matters. *Optics Express* **2015**, 23, 8179–8189.
- (20) Lehmuskero, A.; Johansson, P.; Rubinsztein-Dunlop, H.; Tong, L.; Kall, M. Laser trapping of colloidal metal nanoparticles. *ACS Nano* **2015**, *9*, 3453–3469.
- (21) Hajizadeh, F.; S.Reihani, S. N. Optimized optical trapping of gold nanoparticles. *Optics Express* **2010**, *18*, 551–559.
- (22) Ng, L. N.; Luff, B. J.; Zervas, M. N.; Wilkinson, J. S. Forces on a Rayleigh particle in the cover region of a planar waveguide. *Journal of Lightwave Technology* **2000**, *18*, 388–400.

- (23) Ng, L. N.; Zervas, M. N.; Wilkinson, J. S.; Luff, B. J. Manipulation of colloidal gold nanoparticles in the evanescent field of a channel waveguide. *Applied Physics Letters* **2000**, *76*, 1993–1995.
- (24) Zhan, Q. Trapping metallic Rayleigh particles with radial polarization. *Optics Express* **2004**, *12*, 3377–3382.
- (25) Seol, Y.; Carpenter, A. E.; Perkins, T. T. Gold nanoparticles: enhanced optical trapping and sensitivity coupled with significant heating. *Optics Letters* **2006**, *31*, 2429–2431.
- (26) Dienerowitz, M.; Mazilu, M.; Dholakia, K. Optical manipulation of nanoparticles: a review. *Journal of Nanophotonics* **2008**, 2, 021875.
- (27) Cizmar, T.; Romero, L. C. D.; Dholakia, K.; Andrews, D. L. Multiple optical trapping and binding: new routes to self-assembly. *Journal of Physics B: Atomic, Molecular and Optical Physics* **2010**, *43*, 102001.
- (28) Mirsadeghi, S. H.; Young, J. F. Ultrasensitive diagnostic analysis of Au nanoparticles optically trapped in silicon photonic circuits at sub-milliwatt powers. *Nano Letters* **2014**, *14*, 5004–5009.
- (29) Urban, A. S.; Carretero-Palacios, S.; Lutich, A. A.; Lohmuller, T.; Feldmann, J.; Jackel, F. Optical trapping and manipulation of plasmonic nanoparticles: fundamentals, applications, and perspectives. *Nanoscale* **2014**, *6*, 4458–4474.
- (30) Wright, A. J.; Richens, J. L.; Bramble, J. P.; Cathcart, N.; Kitaev, V.; O'Shea, P.; Hudson, A. J. Surface-enhanced Raman scattering measurement from a lipid bilayer encapsulating a single decahedral nanoparticle mediated by an optical trap. *Nanoscale* 2016, 8, 16395–16404.
- (31) Melzer, J. E.; McLeod, E. Fundamental limits of optical tweezer nanoparticle manipulation speeds. *ACS nano* **2018**, *12*, 2440–2447.

- (32) Draine, B. T.; Goodman, J. J. Beyond Clausius-Mossotti: wave propagation on a polarizable point lattice and the discrete dipole approximation. Astrophysical Journal 1993, 405, 685–697.
- (33) Novotny, L.; Hecht, B. Principles of nano-optics; Cambridge University Press, 2012.
- (34) Born, M.; Wolf, E. Principles of optics: electromagnetic theory of propagation, interference and diffraction of light; Elsevier, 2013.
- (35) Balanis, C. A. Antenna theory: analysis and design; John Wiley & Sons, 2005.
- (36) Johnson, P. B.; Christy, R. W. Optical constants of the noble metals. *Physical Review B* **1972**, *6*, 4370–4379.

TOC Graphic

